UNIVERSITY OF OKLAHOMA

GRADUATE COLLEGE

NON-TERMINAL HYDROMETEOR FALL SPEED EFFECTS ON MODELED RAIN PROCESSES

A THESIS

SUBMITTED TO THE GRADUATE FACULTY

in partial fulfillment of the requirements for the

Degree of

MASTER OF SCIENCE

By

LOGAN M. ROY
Norman, Oklahoma
2023

NON-TERMINAL HYDROMETEOR FALL SPEED EFFECTS ON MODELED RAIN PROCESSES

A THESIS APPROVED FOR THE
SCHOOL OF METEOROLOGY

BY THE COMMITTEE CONSISTING OF

Dr. Gregory McFarquhar, Chair

Dr. Feng Xu

Dr. Hugh Morrison

Acknowledgments

I would like to begin by thanking my advisor Dr. Greg McFarquhar. Without his continuous support, guidance, and encouragement, I would not have grown as a scientist and would not have been able to complete this project. I am extremely grateful for the commitment you showed me and hope that I can carry all the lessons you taught me into my future work.

I would also like to thank Dr. Feng Xu, without whom it would have been impossible to complete this project. Your work managing the logistics of this project was invaluable and for that, I am truly grateful. I'd also like to thank Dr. Hugh Morrison whose expertise has inspired me to take this research as far as I can and share it with as many members of the cloud modeling community as will listen.

I would like to thank Dr. Wei Wu, who initially supported my master's research. Without his faith in my abilities, I would not have had the opportunity to grow through this research. While it wasn't possible to finish the research under his guidance, he has continued to go above and beyond in supporting me, and for that, I am extremely grateful

For all the members of OU and the cloud modeling community that have supported and helped me grow as a scientist, I am so thankful.

Lastly, I must acknowledge the tremendous support I received from my loving family. Without their encouragement, I would never have been able to push myself in my academic career. I want to specifically thank my sister, Alex Roy, for giving up

her guest bedroom for 2 years. Without your support I would not have been able to do any of this. Thank you all so much.

Table of Contents

List of Tables

List of Figures

Abstract

Recent observational studies have shown hydrometeors exhibit non-terminal fall speeds. The goal of this study is to understand how these non-terminal fall speeds affect the collision, coalescence and breakup of raindrops in a Lagrangian cloud model called the Cloud Particle Model (CPM). The observational studies identified three important characteristics of the non-terminal fall speeds; 1) hydrometeor fall speeds have some variance around the expected terminal velocity; 2) hydrometeors have a tendency for large particles (D $>$ 1.5 mm) to display sub-terminal fall speeds and small particles (D $<$ 0.5 mm) to display super-terminal fall speeds; 3) hydrometeors have the tendency for large particles to have narrower fall speed distributions than small particles. The CPM is a Lagrangian model that uses the method of limited volume (MLV) to maintain computational feasibility rather than the super droplet method commonly used in Lagrangian models. The MLV samples a fixed number of nearby particles at each time step to calculate collisional interactions rather than combine multiple particles of the same size into super droplets. This makes the CPM more sensitive to random fluctuations than the super droplet method, a desirable feature for studying random variation in fall speeds.

The first sensitivity study, varying the width of the fall speed distribution, showed that there was a critical width of the velocity variations, which if not exceeded, resulted in approached equilibrium distributions that were statistically indistinguishable from the equilibrium distributions approached using the deterministic terminal velocities. The exact value of this critical standard deviation depends strongly on the assumed initial distribution. The second sensitivity test, adding a bias term, showed the bias had a greater impact on the number concentration of large particles in the

approached equilibrium distribution than the did random noise term, which means the bias has a big impact on higher moments of the size distribution like radar reflectivity and rain rate. The last sensitivity study, which scaled the variance of large particles, found that the scaling term had a very small effect on any moment of the approached equilibrium distribution, including the number concentration (7 % change between scaling terms, and 18 % change between bias terms) and rain rate (1.3 % change between scaling terms and 5 % change between bias terms), which lessens the impact of the term compared to the other two terms.

Chapter 1

Introduction and Background

Improvements in modeling of cloud microphysical processes can impact a wide range of fields from numerical weather prediction and radar retrievals to hydrology. Clouds represent a major source of uncertainty in climate models and are important to numerical weather prediction through radiative effects and latent heat release. Corrections to the drop size distributions, specifically functional fits to environmental variables could be used to modify the assumed DSD in radar retrieval algorithms to more accurately interpret the radar signal. Currently, Satellite platforms like the GPM and before it the TRMM used cloud models based on bulk schemes to generate statistics for precipitation retrieval algorithms. The DSD assumed by these applications follows an exponential distribution which has the advantage of being computationally easy to work with but doesn't match the observed DSDs from ground-based or airborne observations. Therefore improved understanding of drop size distributions (DSDs) and their dependence on environmental conditions could improve radar retrieval algorithms (Pei et al., 2014) as well as impact hydrological models and erosion estimations (Rosewell,

1986). This wide application of cloud microphysics necessitates a robust understanding of the underlying mechanisms that affect the DSDs which is still lacking.

1.1 Cloud Microphysics Modeling Basics

Three major types of cloud microphysics models are currently used, bulk schemes, bin schemes, and Lagrangian schemes. Bulk schemes offer computational efficiency at the expense of microphysical detail, as they require assumptions about the shape of the DSD and cannot generally offer insight into DSD development due to these assumptions (Grabowski et al., 2019). Bin schemes represent DSDs as discrete distributions where the mass and number concentrations are predicted for specific size bins, allowing the distribution to evolve under the influence of various microphysical processes. Thus, bin schemes offer much more detail than bulk schemes and allow for the study of DSD development. But, bin schemes suffer from numerical diffusion, mean-field theory approximations of microphysical processes, and the curse of dimensionality, which pose a challenge to accurately modeling DSD development (Tzivion et al., 1987; Morrison et al., 2018; Grabowski et al., 2019). Lagrangian models have recently been adopted as an alternative to bin schemes, offering similar levels of micropysical detail, without the draw back of numerical diffusion. These schemes operate by representing DSDs as a collection of Lagrangian particles, which are tracked as they advect through a domain without numerical diffusion. Lagrangian schemes are only computationally feasible due to the adoption of the super droplet method (SDM) which uses the concept of superdroplets to represent a large number of real droplets of the same size (Andrejczuk et al., 2008; Shima et al., 2009; Andrejczuk et al., 2010). There are still drawbacks

associated with Lagrangian schemes beyond their computational cost, including ambiguity in the number of super droplets that are required within a grid box to accurately represent the microphysical properties in various conditions, and the problem of activating additional super droplets. One common approach to use models to study DSDs is to allow the development of a steady state under some set of conditions, usually in a box model, and perform sensitivity studies to understand the impact of various microphysical processes or environmental conditions on the steady state DSD that is approached (Srivastava, 1971, 1982; List and McFarquhar, 1990; McFarquhar, 2004; Young, 1975; Hu and Srivastava, 1995).

One of the main microphysical processes responsible for warm rain development is the collision-coalescence processes, which is described by the stochastic collection equation (SCE), sometimes known as the Smoluchowski equation, which is given by

$$\frac{\partial n(v,t)}{\partial t} = -n(v,t)\int_0^{+\infty} K(v,u)n(u,t)\,du + \frac{1}{2}\int_0^{v} K(u,v-u)n(u,t)n(v-u,t)\,du + \int_0^{+\infty} L(v,u)n(u,t)\,du - \frac{n(v,t)}{v}\int_0^{v} uL(v,u)\,du + SC(v,t) - SK(v,t), \quad (1.1)$$

where $n(v,t)$ is the number distribution for particles of volume v at time t, $K(v,u)$ is the collection kernel, $L(v,u)$ is the breakup kernel, and $SC(v,t)$ and $SK(v,t)$ are source and sink terms (Gillespie, 1972, 1975). Several attempts have been made to represent DSDs using analytical functions with several forms, including exponential distributions (Marshall and Palmer, 1948), gamma distributions (Ulbrich, 1983), and log-normal distributions (Feingold and Levin, 1986). However since the stochastic collection equation cannot be solved analytically except for simple collection kernels, these analytical functions do not fully represent the evolution of the DSD (Scott, 1968;

Drake, 1972; Schumann, 1940). To address the lack of analytical solutions, bin schemes are implemented to understand the development of DSDs. Despite its name, the SCE is actually deterministic, relying on the mean field approximations of particle collisions to represent the physical processes, which is fundamentally stochastic (Grabowski et al., 2019). The mean-field approach of the SCE used in bin schemes is unable to represent the random fluctuations of the stochastic collision-coalescence processes, which are important for "lucky droplet" theories (Dziekan and Pawlowska, 2017), which cannot be tested or simulated using bin schemes.

Lagrangian schemes actually calculate the probability of two droplets interacting from the collision kernel and determine the outcome of the interaction using these probabilities in collection and breakup kernels, which makes them ideal for understanding the importance of the stochastic coalescence-breakup process. Lagrangian schemes that use the SDM can capture the stochastic nature of the coalescence-breakup process, but still suffer from mean approximations associated with the multiplicity of super droplets. The effects of the mean field approach used in bin schemes and the super droplet method used in Lagrangian schemes extends to more than just the stochastic coalescence-breakup process, but to all stochastic properties of cloud microphysics. To address the limitations of these schemes, a new model was developed by Dr. Wei Wu, the Cloud Particle Model (CPM), which is used to study the impact of stochastic variables on DSD development. The CPM is a particle based model capable of directly simulating the growth of individual particles, which leverages the utility of Lagrangian models, without suffering from sampling issues associated with the super droplet method. The representation of particle fall speeds in Lagrangian models is the focus of the research presented here, but it is also identified that the supersaturation is

a potentially important stochastic variable in the representation of cloud microphysics (Chandrakar et al., 2021).

1.2 Non-Terminal Hydrometeor Fall Speeds

Several studies have identified particle fall speeds as non-terminal (Bringi et al., 2018; Chatterjee et al., 2022; Montero-Martínez and García-García, 2016; Thurai et al., 2019), however most models still assume that hydrometeors fall at their terminal fall speeds using some form of the Gunn and Kinzer (1949) terminal fall speed measurements. Observations from a two dimensional video disdrometer (2DVD) and an optical array probe by Bringi et al. (2018) measured significantly broadened fall speed distributions for droplets of size 3 mm, 2 mm , and 1.3 mm with negative skewness, meaning sub-terminal droplets were more common than super-terminal droplets, in high intensity turbulence during heavy rainfall. Montero-Martínez and García-García (2016) observed droplet fall speeds under calm, light, and moderate wind conditions and under different rain rates. They observed super-terminal fall speed for particles of size less than 0.7 mm and sub-terminal fall speeds for particles up to 2 mm. They identified a correlation with increasing wind intensity and increasing departure from terminal velocities. These results led them to conclude that more turbulent conditions lead to a general broadening of hydrometeor fall speeds for particles of various sizes. Thurai et al. (2019) also observed sub-terminal droplet fall velocities for particles of sizes larger than 2 mm. These studies attribute the observed sub-terminal fall speeds mostly to the oscillation of the larger droplets cross sectional area resulting in an increased drag coefficient in more turbulent conditions. This explanation has been tested in direct

numerical simulations of water droplets in turbulent flows by Ren et al. (2020). They found that the difference in oscillation amplitude was not significantly affected by the presence of turbulence and could not fully explain the difference between fall speeds in still vs turbulent conditions. Instead they presented the decrease in wake recirculation length as the key factor to increased drag coefficients for droplets in turbulent conditions. Independent of the exact nature or cause of the sub-terminal fall speed, the DNS study by Ren et al. (2020) produced results similar to those observed by the studies mentioned above.

Larsen et al. (2014) presented observations which confirm earlier observations of super-terminal droplets using an array of laser precipitation monitors and a 2DVD to observe 6 rain cases. The array of laser precipitation monitors observed a significant proportion of droplets, between 80% and 5% depending on the size of particles, with diameters less than 1 mm with super-terminal fall speeds, in agreement with past studies. Another study by Chatterjee et al. (2022) used optical laser based disdrometers to observe the size and velocities of particles during a large number of rain events. They observed sub-terminal velocities for droplets of sizes greater than 1 mm. Particles of sizes between 0.6 mm and 1.1 mm displayed some super-terminal (faster than terminal) and some sub-terminal (slower than terminal) fall speeds with a strong negative bias. For particles of sizes less than 0.6 mm the bias shifts from negative to positive.

There are several proposed hypotheses to explain the observed super-terminal fall speeds (Ren et al., 2020; Chatterjee et al., 2022; Larsen et al., 2014). Firstly, the super-terminal droplets may be the resultant fragments of very recent breakup events of larger droplets. In this explanation the super-terminal fall speed is highly transitory and the droplets return to the expected fall speed after some relaxation time due to

drag forces. The second hypothesis invokes wake effects to explain the supper-terminal fall speeds, where small particles are pulled along in the wake of a larger droplets, resulting in fall speeds greater than expected. The third hypothesis states that the oscillations of the droplets cross sectional area results in different drag coefficients, which lead to non-terminal fall speed observations. The last hypothesis attributes the super-terminal fall speeds directly to turbulent effects, where smaller particles with lower inertia are more directly influenced by turbulent eddies resulting in fall speed deviations having a strong dependence on particle size.

It is hypothesized that the strictly terminal treatment of hydrometeor fall speed leads to under representing collisional activity and strictly precludes the collisional interaction of particles of similar sizes, which would be possible when non-terminal fall speeds for particles are allowed. Past DNS studies have identified similar particle interactions as a consequence of turbulence. This thesis test this hypothesis using the Cloud Particle Model.

The model is described in section 2, then in section 3 several sensitivity studies are presented where the effects of fall speed distribution biases and variance, as well as hydrometer inertia on the DSD development, is described. Finally in section 4 the major findings of this study are discussed and summarized along with several suggestions for future work.

Chapter 2

The Cloud Particle Model

The CPM is a new particle based microphysics model for warm rain microphysics that was developed by Dr. Wei Wu to understand important impacts on non-mean-field effects on DSDs. Currently the CPM is limited to warm rain processes and will be extended to include ice phase and mixed phase processes in the future. The CPM includes several microphysical processes implemented on a particle by particle basis which allows for a careful analysis of non-mean-field effects when compared with Lagrangian models which are limited by the sampling bias of the super droplet method. The microphysical processes that are represented in the CPM include diffusional growth, collision-coalescence, collision induced breakup, and spontaneous breakup. Stochastic representation of two microphysical properties, hydrometoer fall speed and super saturation, have been identified as particularly promising for investigating the impact of non-mean microphysical properties on DSD development. This study focuses on the impact of stochastic fall speed because of its importance to the collision induced coalescence and breakup of particles. It is important to note that the stochastic representation of super saturation has the potential to impact the diffusional growth of

particles, and hence DSD development as well. The following subsections describe the treatment of each microphysical processes that is implemented in the CPM.

2.1 Processes

2.1.1 Diffusional Growth

The growth of droplets by diffusion of water vapor onto droplets is modeled following Pruppacher and Klett (2010), with

$$r(t+\Delta t) = \sqrt{r_0^2 + \Delta t \left(\frac{1}{F_d + F_k} \left(4 * SS - \frac{8a}{r_0} + \frac{32b}{r_0^3} \right) \right)} \tag{2.1}$$

where r is the radius of the particle at time $t + \Delta t$ and r_0 is the radius at time t, Δt is the time step used in the simulation, SS is the supersaturation, and F_d and F_k are the vapor diffusion and thermodynamic conduction terms, respectively, given by

$$F_d = \frac{\rho RT}{2re_s(T)}, \tag{2.2}$$

where ρ is the density of liquid water, R is the specific gas constant of water vapor, T is temperature, and $e_s(T)$ is the vapor saturation pressure over a plane surface of water at temperature T, and

$$F_k = \frac{(L/RT - 1) * L\rho}{KT}, \tag{2.3}$$

where L is the latent heat of vaporization of water, and K is the coefficient of thermal conductivity of air. The a parameter is given by

$$a = \frac{2M_w\sigma}{RT\rho} \tag{2.4}$$

where M_w is the molecular weight of water, σ is the surface tension of water, and b is given by

$$b = \frac{m_s i M_w}{M_s(4/3\pi\rho)} \tag{2.5}$$

where m_s is the mass of solute, i is the Van 't Hoff disassociation factor, and M_s is the molecular weight of the solute.

2.1.2 Coalescence

To model the coalescence of two droplets in the CPM a geometric kernel is used to determine the probability that two droplets collide during a time step. Each particle falls some distance in each time step, and has a probability to interact with the particles it sweeps out in that time step as a function of the diameter of both droplets, and their fall speeds. This probability of collision, $P(coll)$, is calculated as

$$P(coll) = E * G(r_1, r_2, V_1, V_2, Vol) * \Delta t \tag{2.6}$$

where E is the collision efficiency which is a constant in the CPM and G is the geometric collision kernel, which is calculated as

$$G(r_1, r_2, V_1, V_2, Vol) = \frac{|V_1 - V_2|\pi(r_1 + r_2)^2}{Vol} \tag{2.7}$$

where r_1 and r_2 are the radii of the particles, V_1 and V_2 are the velocities of the particles, and Vol is the volume of the simulation. If the two particles do collide, then one of two processes ensues: coalescence or breakup. To determine the outcome of collisions, a probability for the particles to coalesce is calculated following Low and List (1982) as

$$P(coal) = \frac{\frac{a}{exp(b\sigma * ET^2/SC)}}{(1 + D_1/D_2)^2} \tag{2.8}$$

where the constants a = 0.778 and b = 2.61 $X10^6 J^{-2} m^2$, σ is the surface tension of water, ET is the total energy of coalescence, SC is the energy associated with the surfaces of the two interacting particles, and D_1 and D_2 are the diameters of the particles. Note that in this equation it is important that $D_1 < D_2$, and that all velocities used for these equations use the actual non-terminal fall speed, rather than the terminal fall speed that is typically used in the application of these equations.

2.1.3 Collisional Breakup

Like coalescence, collision induced breakup is handled probabilistically in the CPM. The probability of breakup is the complement of the probability of coalescence meaning when two particles collide, if they don't coalesce, then they must breakup. The fragment size distributions produced by collision induced breakup are represented following the McFarquhar (2004) parameterization where three types of breakups can occur, filament, sheet, or disk. The fragment distribution is represented by a combination of Gaussian and gamma distributions from which the resultant fragment particles are drawn probabalistically while insuring mass conservation. For all breakup types the number of fragments produced, and the distribution from which they are sampled are a function of the sizes of the two colliding droplets. More details about the implementation of this parameterization can be found in McFarquhar (2004). To conserve mass in collisional breakup events, tests insure that the particles generated have the same mass as that of the two colliding particles.

2.1.4 Spontaneous Breakup

The CPM models spontaneous breakup of particles following Komabayasi et al. (1964) which describes the probability that a particle of size D will spontaneously breakup in a given time step, Δt, $P(r, \Delta t)$ as

$$P(r, \Delta t) = \Delta t * (2.94^{-7}) * e^{68*D}. \tag{2.9}$$

Once a particle undergoes spontaneous breakup the resultant distribution of fragment droplets is assumed to follow an exponential distribution with scale parameter set as one seventh the parent droplet size. This process is not very active compared to the other processes, occurring only when droplets grow to a size greater than 5.5 mm.

2.1.5 Limited Volume Method

The CPM does not use the super droplet method to limit the computational cost of the simulations; instead it uses the limited volume method (LVM). The LVM limits the amount of particle pairs checked at each time step in the collision processes to some constant A. This results in a computational cost on the order of $O(AN)$ rather than $O(N^2)$, which results in significantly lower computational cost for simulations with N on the order of 10^9 particles. For these simulations A was set to 1000, following Dziekan and Pawlowska (2017). Initial testing of the CPM by Dr. Wu indicates that increasing values of A converge in agreement with Dziekan and Pawlowska (2017).

2.2 Stochastic Fall Speed

The usual representation of hydrometeor fall speeds is done following some fit to the data collected by Gunn and Kinzer (1949). In this study the fit described by Foote and Toit (1969) to the Gunn and Kinzer (1949) data is used to represent what is called the terminal fall speed of droplets, which is given by

$$V_{Terminal} = [-0.193 + 4.96D - 0.904D^2 + 0.0566D^3]e^{\frac{z}{20}}. \tag{2.10}$$

Simulations with this fall speed representation will serve as a control run to compare the various representations of non-terminal fall speeds.

Several different representations of non-terminal fall speeds are implemented in this study. The simplest form of non-terminal fall speed is a simple stochastic noise term, described further in section 2.2.1, added to the terminal fall speeds calculated using equation 2.10. The other representations each consider a specific physical feature of non-terminal fall speeds, whether that feature is observed in ground based studies like Montero-Martínez and García-García (2016), Bringi et al. (2018), Testik and Bolek (2023), or Chatterjee et al. (2022), or is expected from the physical sources of non-terminal fall speeds as explained in these studies. These features include observed biases and variance in non-terminal fall speeds, and the inertia of hydrometeors.

2.2.1 Simple Noise Term

The simple stochastic noise term is the simplest representation of non-terminal fall speeds, and calculates hydrometeor velocities as

$$V_{Simple} = [-0.193 + 4.96D - 0.904D^2 + 0.0566D^3]e^{\frac{z}{20}} + \epsilon \tag{2.11}$$

where ϵ is the Gaussian noise term,

$$\epsilon = N(\mu = 0, \sigma) \tag{2.12}$$

with a mean of μ and variance of σ. It is important to note that this term is uncorrelated in time and across particles which likely over represents the number of collisions.

Even with this simple representation there is an important characteristics of model behavior under non-terminal fall speeds that can be studied, the model sensitivity to the width of the fall speed distribution, which is represented by the standard deviation of the noise term, σ. Observations from Montero-Martínez and García-García (2016), Bringi et al. (2018), Testik and Bolek (2023), and Chatterjee et al. (2022) found hydrometeors with fall speed distributions around the terminal velocity calculated from equation 2.10. The exact standard deviation for any given particle size is poorly constrained from these studies but the observed standard deviations range from 0.5 m/s $< \sigma <$ 1.5 m/s. Also, the existence of a distribution is consistent for observations in windy conditions.

2.2.2 Bias

The same studies that observed non-terminal fall speeds also identified strong relationships between observed fall speed distribution bias and particle size (Bringi et al., 2018; Chatterjee et al., 2022; Montero-Martínez and García-García, 2016). Specifically these studies found that particles larger than 1.3 mm had negative biases (lower fall speed than expected from Gun and Kinzer data) while particles less than 0.8 mm had positive biases (higher fall speeds than expected from Gun and Kinzer data). The physical cause of the observed bias in fall speeds is still poorly constrained but there

are a few different theories presented in the observational studies: Firstly, Bringi et al. (2018) and Montero-Martínez and García-García (2016) note that the magnitude of the fall speed bias is correlated with the strength of the wind associated with each observation. This led Montero-Martinez and Garcia Garcia to present a turbulence-based explanation for the presence of the bias, with large and small particles preferentially interacting with different vertical regions of turbulent eddies. The DNS study by Ren et al. (2020) observed the sub-terminal fall speed bias in large droplets and identified the underlying cause as increased drag interactions in the presence of turbulence.

However, these studies were limited in the maximum and minimum sizes of raindrops that were observed. Extending this general relationship to larger and smaller diameters can be accomplished by adding in a functional dependence of the bias of the noise term on the particle size. While the observations provide good agreement on the general trend of super-terminal small droplets and sub-terminal large droplets, the exact nature of the bias dependence on size is still poorly constrained. To represent this trend in the CPM the fall speeds were calculated using

$$V_{Bias} = [-0.193 + 4.96D - 0.904D^2 + 0.0566D^3]e^{\frac{z}{20}} + [\epsilon(\mu(D), \sigma)] \tag{2.13}$$

where $\mu(D)$ is

$$\mu(D) = -2.\overline{6}e^{-4}D + 0.25. \tag{2.14}$$

Equation 2.14 is a rough linear fit that captures the negative bias for large particles and the positive bias for small particles. This linear function was selected such that the bias for particles between 0.8 mm and 1 mm was close to zero, while the positive and negative biases for particles with diameters near zero and particles with diameters near 2.5 mm was +0.25 m/s and -0.4 m/s respectively. The function $\mu(D)$ is a crude

first order approximation to the observations, specifically chosen as a conservative approximation that can demonstrate how this bias tendency affects model behavior.

2.2.3 Scaling

The first extension to the simple noise term representation is to include the effects of the inertia of the particles on the non-terminal fall speed term. This is represented as a scaling factor, S(D), applied to the standard deviation in the noise term

$$V_{tScale} = [-0.193 + 4.96D - 0.904D^2 + 0.0566D^3]e^{\frac{z}{20}} + [\epsilon(\mu, \sigma * S(D)] \tag{2.15}$$

where S(D) is the scaling factor. S(D) is defined as

$$S = \begin{cases} \sqrt{\frac{D_s}{D}}, & \text{if } D \geq D_s \\ 1, & \text{otherwise} \end{cases} \tag{2.16}$$

where D_s is defined as the scaling diameter. By varying D_s the study of the model dependence on σ can be extended to include the tendency of larger droplets to have smaller fall speed distribution widths than smaller droplets, as observed in several ground based studies.

2.3 Statistical Methods

For this study, a bootstrap technique was applied to evaluate and compare a wide array of relevant statistics to various combinations of model outputs. To determine if two DSD's statistics are significantly different from one another, the following statistical analysis was performed, following Rousselet et al. (2021).

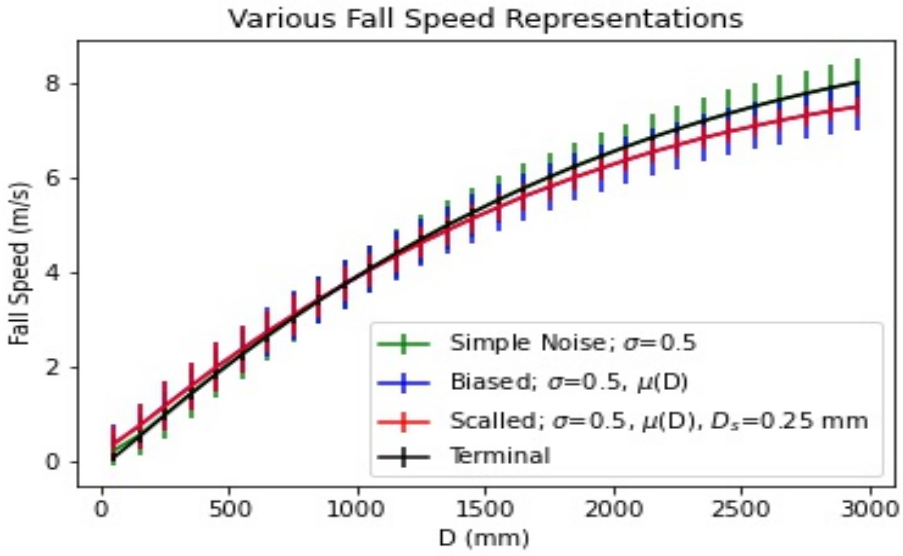

Figure 2.1: Comparison between the different types of fall speeds available to the CPM, terminal in black, simple noise in green, biased in blue, and scaled in red.

1. Each DSD was sampled with replacement 10,000 times to generate two "synthetic data sets".

2. Some relevant statistic was calculated for each of the synthetic data sets.

3. The ratio of these synthetic statistics was recorded.

4. Steps 1-3 were repeated 10,000 times to generate a histogram of synthetic statistic ratios.

5. Percentiles associated with the 97.5% and 2.5% were identified for the histogram of synthetic statistic ratios.

6. If 1.0 was not between the bounds identified in step 5, the two distributions were identified as significantly different at the α=0.05 level.

The specific statistic calculated for each of the synthetic data sets is flexible enough to allow this analysis to be applied to various data sets with different statistics. This flexibility is very useful for the multiple sensitivity studies presented in section 3. Several classes of statistics are used, including DSD moments, velocity statistics, and collision statistics. The most commonly evaluated DSD moments are the zeroth moment, which is equivalent to the number concentration (N_0) and the third moment, which is equivalent to the liquid water content (LWC). The rain rate (RR) is also useful for characterizing the distributions. The velocity statistics used in this analysis were the mean and standard deviation, and the collision data used to determine whether two model runs were significantly different was the total number of collision events, and the ratio of coalescence events to breakup events.

Chapter 3

Sensitivity Studies

To better understand the effects of non-terminal fall speeds on model output and behavior, several different sensitivity studies were preformed. The variables tested include both the standard deviation (σ) and bias (μ) of ϵ in equations 2.11 and 2.15, and the inertial scaling parameter, D_s in equation 2.16. The total number of particles simulated for each run was on the order of 10^8. The CPM is largely memory limited by the volume of the simulation. For our purposes, a simulation volume of 20 m^3 was used. The simulations were run on the NCAR Cheyenne supercomputer utilizing the large memory nodes to maximize the volume simulated (Computational and Information Systems Laboratory, 2020). It is possible to trivially parallelize the CPM by running multiple simulations with identical initializations to simulate larger and larger volumes. However, it is difficult to parallelize the simulation to account for the vertical or horizontal inhomogeneity needed for accurate modeling of real cases. First, several model runs were performed using different standard deviations for the noise term to determine how wide the noise distribution can get before there is a statistically significant impact on model output. Second, a bias was added to the noise

term ϵ that approximated the behavior of particles as observed in ground based studies to determine the impact of large droplets tendency to fall at sub-terminal fall speeds and small droplets tendency to fall at super-terminal fall speeds on model behavior. The last sensitivity test involved varying D_s in equation 2.16 to determine the model sensitivity to inertial tendencies.

3.1 Stochastic Sensitivity

Measured distributions of particle fall speeds reported in Bringi et al. (2018) and Testik and Bolek (2023) show a dependence on particle size and wind speed, but generally constrain the standard deviation of the distributions to within ±2 m/s for particles with 0.5 mm < D <1.3 mm, with less variance for particles with D > 1.3 mm. For this sensitivity study, the standard deviation (σ) of the normal distribution from which the noise term of the non-terminal fall speed is sampled is varied from σ = 0 m/s to σ = 0.5 m/s with σ being the same regardless of particle size. These standard deviations are tested by running identical model setups 10 times for each variance to generate statistics to compare model output behavior under different amounts of noise. For the initial stochastic sensitivity test, an exponential distribution

$$N(D) = N_0 \lambda e^{-\lambda D} \tag{3.1}$$

with total number concentration $N_t = 6000\ m^{-3}$ and mean particle size $\lambda = \frac{1}{550}\ \mu\text{m}^{-1}$ is sampled to generate the initial distribution. The DSDs development under different standard deviations over the course of one hour are plotted in Figure 3.1. After 3600 s there were no large changes in the shape of the DSD, therefore the distribution at 3600 s was identified as the approached equilibrium distribution.

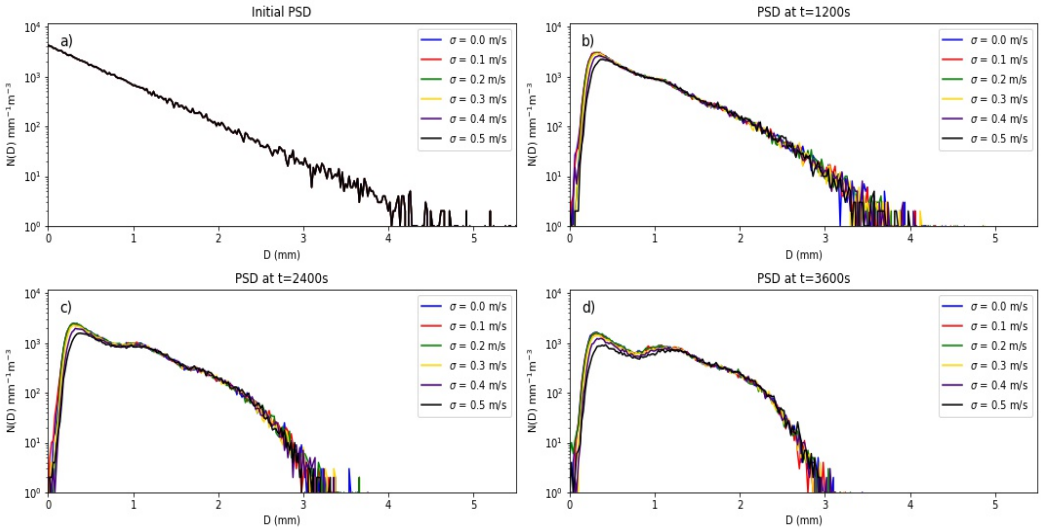

Figure 3.1: DSD evolution in a box model from an initial exponential distribution for each of the different σ values tested at four different times during the evolution towards equilibrium. The most obvious difference between the runs is the decrease in number concentration of particles with diameters less than 1.3 mm. The plots show the distributions at different time: a) t = 0 s; b) t = 1200 s; c) 2400 s; d) t = 3600 s

The difference between the DSDs for different σ as time evolves is most apparent in the decrease in number concentration of particles with diameters less than 1.3 mm as time evolves, with the equilibrium distribution approached with $\sigma = 0.5$ m/s only having 78% as many particles with diameters less than 1.3 mm as the equilibrium distribution approached with $\sigma = 0.0$ m/s. There is a corresponding increase in particles with D $>$ 1.3 mm but this relationship is less obvious from the DSD plots due to the smaller percent change. For example the $\sigma = 0.5$ m/s run had 3.5% more particles

with D $>$ 1.3 mm in the equilibrium distribution approached than the $\sigma = 0.0$ m/s run.

A plot of the p-value generated by the bootstrap test for significant differences between the distribution modeled at each time for each σ tested against the distributing at the same time for the $\sigma = 0$ m/s run is shown in Figure 3.2. From Figure 3.2 it is clear that simulations with $\sigma \geq 0.25$ m/s approach equilibrium distributions with diverging bulk properties (the divergent group) compared to the model runs with $\sigma < 0.25$ m/s (the similar group) for simulations initialized with this exponential distribution.

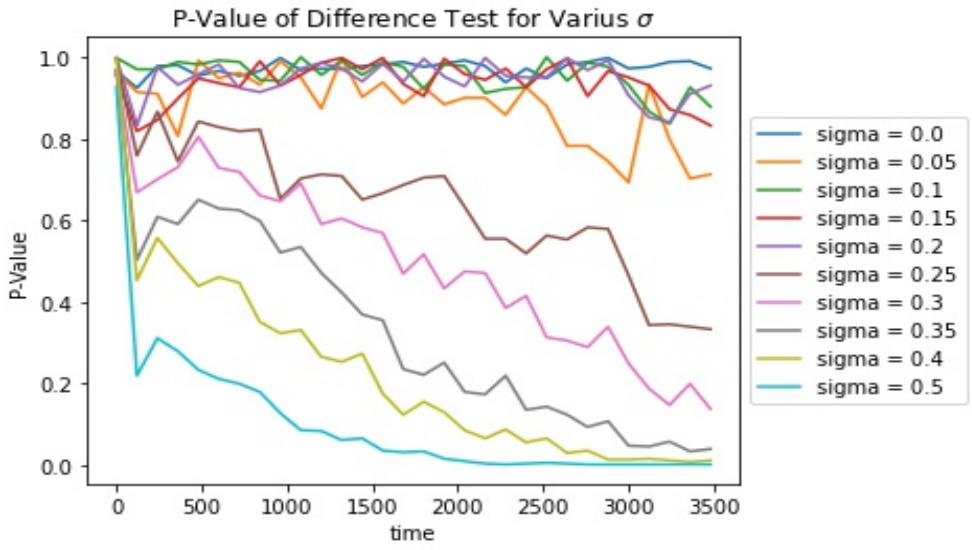

Figure 3.2: P-value generated by the bootstrap statistical analysis comparing each model run to the terminal case ($\sigma = 0$ m/s) as a function of time.

It is important to identify which processes are responsible for the difference between the strictly terminal fall ($\sigma = 0.0$ m/s) speed run and the runs with larger σ to understand the implications of non-terminal fall speeds. Of the processes represented

in the CPM, the only one that is likely to have a strong dependence on fall speed variance is the collision-coalescence-breakup process due to the importance of relative particle velocity for these process. The collision-coalescence-breakup process depends on the relative velocities to calculate the sweep out volume in the geometric kernel, and the kinetic energy is used to calculate coalescence efficiency and fragment size distributions. Comparing the collisional activity (number of collisions per second per particle) is shown in Figure 3.3 shows higher collisional activity in runs with higher σ, thus showing this process is affecting the DSD evolution.

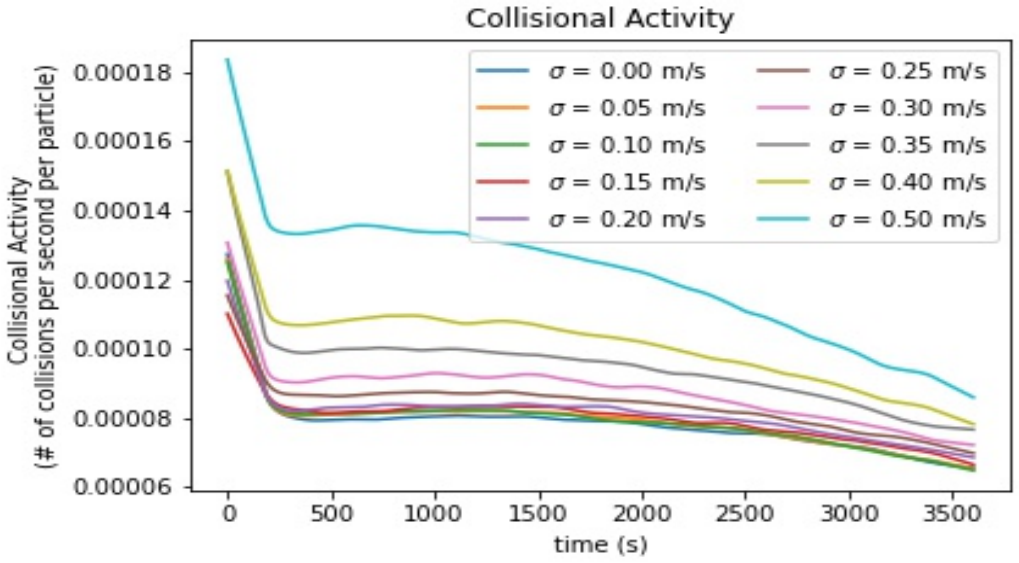

Figure 3.3: Collisional Activity for all σ runs as a function of time.

This increase in collisional activity is especially profound within the first 100 seconds, where the most dramatic shift from the initial exponential distributions towards the equilibrium distribution occurs, as seen in Figure 3.1 b). Understanding how different values of σ affect the evolution of DSDs is critical for identifying scenarios or

cases where the inclusion of non-terminal fall speeds may be important. Thus two different numerical experiments were performed, the first of which involved varying the total number concentration (the N_t experiment), while the second experiment involved varying the form of the initial DSDs (the distribution experiment).

3.1.1 $\mathbf{N_t}$ Experiment

The N_t experiment allowed a comparison of model behavior in cases with different total concentrations of particles without affecting the ratio of the concentration of small particles to large particles. The three initial exponential distributions are all sampled from the same exponential distribution with mean diameter $D_m = 0.55$ mm. Each distribution varies by N_t with low $N_t = 3000\ m^{-3}$, moderate (mod) $N_t = 6000\ m^{-3}$, and high $N_t = 9000\ m^{-3}$, The three initial exponential distributions for the N_t experiment, and their evolution with $\sigma = 0.5$ m/s are shown in figure 3.4.

From Figure 3.4 b), it is clear that initially all three distributions are most dramatically changed for the smallest and largest particles with a noticeable decrease in the number of particles with D $<$ 0.2 mm and D $>$ 3 mm. Once the distributions have approached equilibrium, shown in Figure 3.4 d), each of the two peaks have a spread of number concentrations across all three N_t runs. The peak around D = 0.4 mm has a spread of N(D) values of 540 $mm^{-1}m^{-3}$ between the low N_t and high N_t runs while the other peak around D = 1.3 mm also has a spread of 540 $mm^{-1}m^{-3}$. The spread in N(D) between the peaks is notably smaller, with only 110 $mm^{-1}m^{-3}$ between the low N_t and high N_t runs. The sharp rise in the number of particles present with diameters of 1 mm to diameters of 1.3 mm is indicative of an increase in collision coalescence rates for the higher number concentration case.

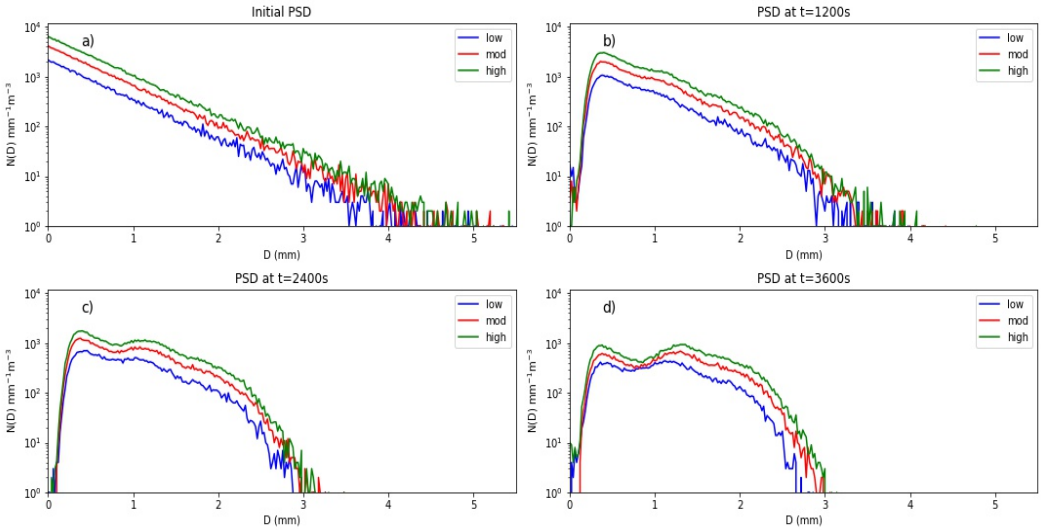

Figure 3.4: DSD development for the three exponential distributions used in the N_t experiment at four times during the equilibrium development with $\sigma = 0.5$ m/s. Low) $N_t = 3000\ mm^{-1}m^{-3}$, mod) $N_t = 6000\ mm^{-1}m^{-3}$, and high) $N_t = 9000\ mm^{-1}m^{-3}$. The plots show the distributions at different time: a) t = 0 s; b) t = 1200 s; c) 2400 s; d) t = 3600 s

To determine if two distributions are significantly different from each other, the bootstrap method outlined in section 2.3 is applied to the two distributions. Table 3.1 shows the P-value of the statistical test to determine uniqueness between the DSD of a given σ value and the strictly terminal fall speed ($\sigma = 0.0$ m/s) run for all times during the simulation, initialized with the same N_t value. If two distributions are significantly different at the 95% confidence level, then the P-value of the test will be less than 0.05. The critical standard deviation, σ^*, is the lowest σ value that results in a significantly different distribution from the strictly terminal fall speed case.

Table 3.1: P-values from the bootstrap statistical test against the $\sigma = 0.0$ m/s run. Significantly different model runs are shown in bold. Note that as N_t increases, σ^* also decreases, from $\sigma^* = 0.4$ m/s for the low N_t run to $\sigma^* = 0.35$ m/s for the moderate and high N_t runs.

σ [m/s]	Low N_t	Moderate N_t	High N_t
0.00	0.987	0.997	0.989
0.05	0.708	0.927	0.711
0.10	0.875	0.976	0.478
0.15	0.826	0.844	0.335
0.20	0.664	0.948	0.264
0.25	0.324	0.281	0.230
0.30	0.109	0.124	0.056
0.35	0.065	**0.018**	**0.008**
0.40	**0.006**	**0.002**	**4e-4**
0.50	**2e-4**	**2e-4**	**2e-4**

All three of the number concentrations have similar values of σ^* around 0.35 m/s, with the low N_t run σ^* being slightly larger at 0.4 m/s. Since it is hypothesized that the collision coalescence process is responsible for the difference between the various σ runs, a comparison between the collision statistics for the divergent group ($\sigma \geq 0.25$ m/s) against the similar group ($\sigma < 0.25$ m/s) is presented in Figure 3.5.

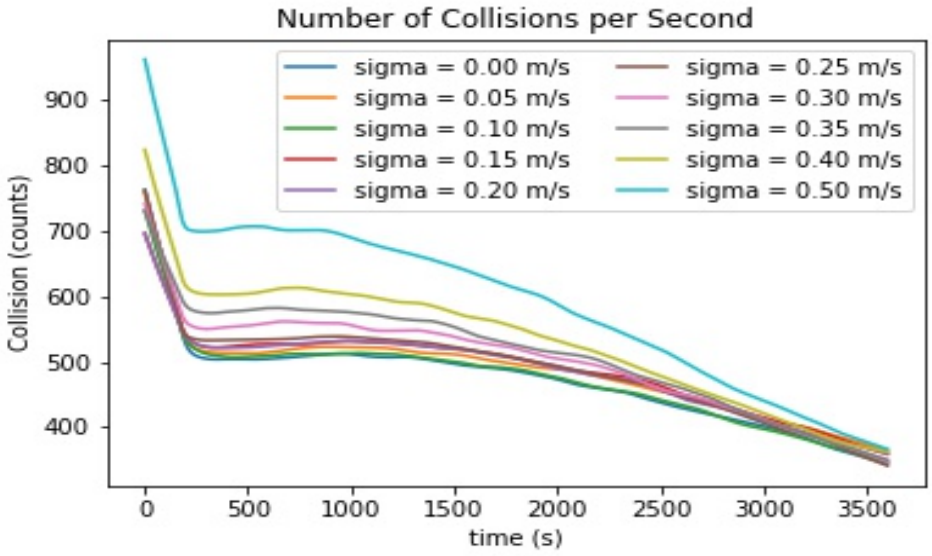

Figure 3.5: Total number of collision events per second for each of the σ values tested with $N_t = 6000\ m^{-3}mm^{-1}$.

From Figure 3.5, an increase in the number of collisions per second with increasing σ is apparent, with the similar group clustering together and the divergent group displaying increase in total collisions by at least 5% of the strictly terminal run. The difference between the total number of collisions is highest after the initial spike in collisions per second, but all models approach the same number of collisions per second by t = 3600 seconds.

A comparison between the number concentration of different size ranges of particles is also performed to better understand how the evolution of DSDs differed for different σ, shown in Figure 3.6. There are four regions of the DSD of interest, the number concentration of the smallest particles with D $<$ 0.15 mm is shown in Figure 3.6 a), this region of the DSD initially drops to near zero where it remains for the duration of

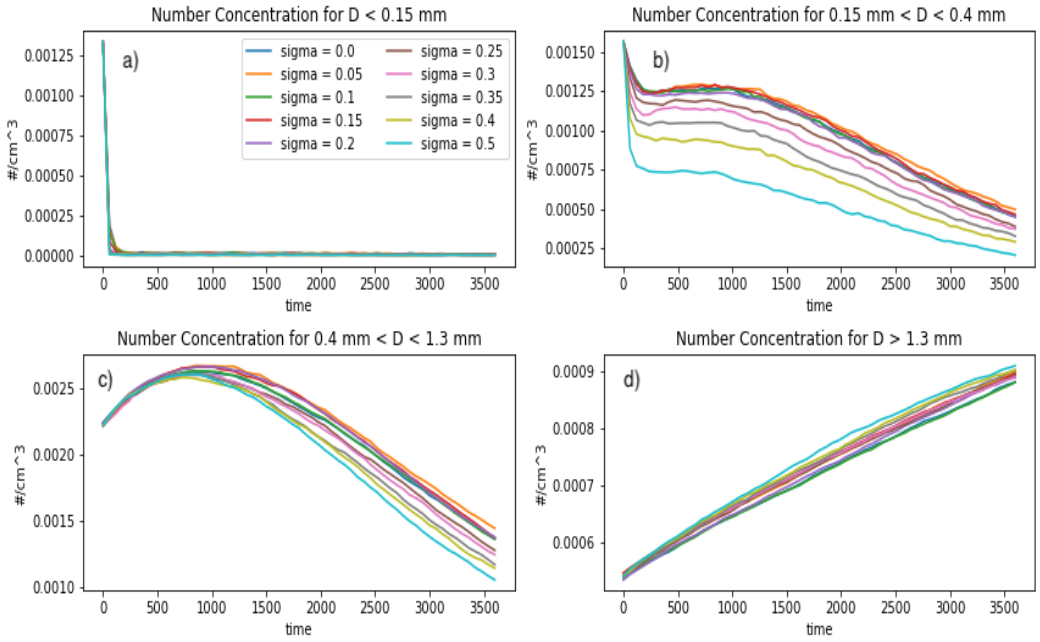

Figure 3.6: The number concentration for various size ranges of particles. Plot a) shows the evolution of number concentration for the region of the DSD which initially experience a complete reduction in particles. Plot b) shows the evolution of number concentration for the region of the DSD populated by particles with smaller diameters than the first peak at D = 0.4 mm. Plot c) shows the evolution of number concentration for the region of the DSD between the two peaks at D = 0.4 mm and D = 1.3 mm. Plot d) shows the evolution of number concentration for the region of the DSD populated by particles with larger diameters than the second peak at D = 1.3 mm.

the simulation for all σ values. Particles with 0.15 mm $<$ D $<$ 0.4 mm, shown in Figure 3.6 b), display different trends depending on the value of σ, the divergent group ($\sigma \geq$ 0.25 m/s) displays a marked decrease in the number concentration of particles in this region of the DSD compared to the similar group ($\sigma <$ 0.25 m/s). The next region of

the DSD of interest is particles with 0.4 mm $<$ D $<$ 1.3 mm is shown in Figure 3.6 c), this region of the DSD shows good agreement between the various σ for the first 500 seconds of the simulation before the divergent group begins producing lower number concentrations than the similar group in this region. The last region of the DSD of interest is for particles with D $>$ 1.3 mm, shown in Figure 3.6 d), where again all of the σ runs result in very similar trends.

The initial drop in number concentration shown in Figure 3.6 a) and b) shows which particles are coalesced in the initial spike in collisional activity shown in Figure 3.5. The difference in the number concentration evolution in Figure 3.6 b) illustrates that with higher σ, larger particles are included in the initial coalescence spike. Since the difference in equilibrium distributions for simulations with varying σ extends to particles with diameters up to 1.3 mm the impact of non-terminal fall speeds should not be ignored in cases where rain rate or liquid water content are of interest even though the greatest difference may be in the smallest particles.

3.1.2 Distribution Experiment

The importance of small particles in determining the evolution of DSDs for different σ values established by the N_t experiment is unsurprising given the dominance of small particles in exponential number concentration distributions. Thus, a sensitivity study using different initial distributions that are not dominated by small particles was performed to explore the role of large particles in affecting the evolution of DSDs. By using three distributions with different fractional importance of small and large particles the relationship between σ^* and the ratio of small to large particles is examined. The three different initial distributions tested were uniform, exponential, and

gamma because there is a large variation in the relative importance of both the total concentration of particles and the ratio of small to large particles.

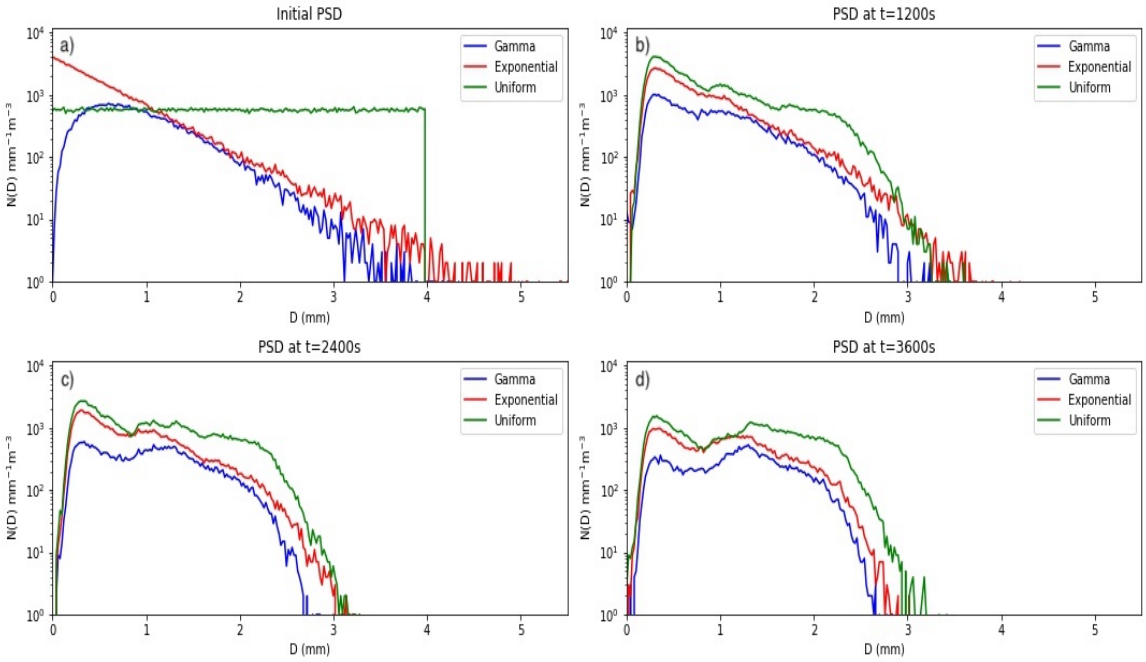

Figure 3.7: The evolution of the three different initial distributions used for the distribution experiment with $\sigma = 0$ m/s at four different times during the simulation. Note that the three distributions in plot d have similar shapes for particles less than 0.8 mm and greater than 1.3 mm, but different shapes for particles of intermediate sizes. The plots show the distributions at different time: a) t = 0 s; b) t = 1200 s; c) 2400 s; d) t = 3600 s

Figure 3.7 shows the evolution of the DSDs from the three different initial distributions with all drops falling at terminal velocity ($\sigma = 0$ m/s). The uniform distribution is initialized using

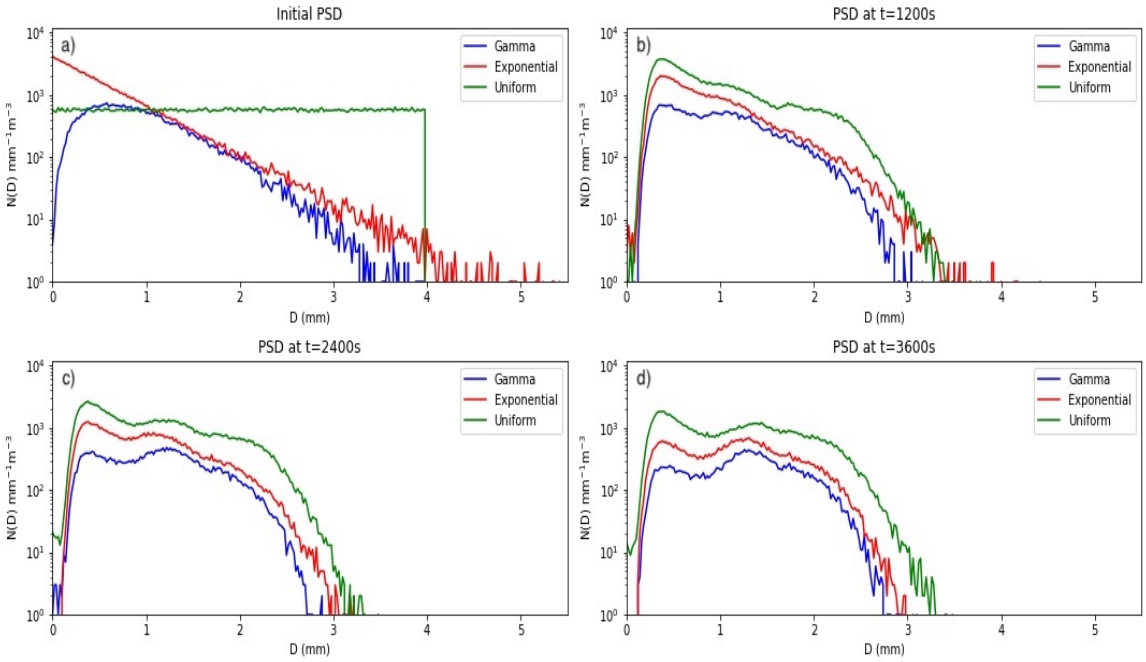

Figure 3.8: Same as figure 3.7 except with $\sigma = 0.5$m/s. Note that in d the different distributions have more similar shapes with $\sigma = 0.5$ m/s than in the model outputs generated with $\sigma = 0.0$ m/s, especially when looking at particle concentrations around 1 mm.

$$N(D) = \begin{cases} 3000, & \text{if } D < 4mm \\ 0, & \text{otherwise} \end{cases} \tag{3.2}$$

and the gamma distribution is initialied using

$$N(D) = \frac{\beta^{\alpha}}{\Gamma(\alpha)} D^{\alpha-1} e^{-\beta D} \tag{3.3}$$

where $\beta = \frac{1}{310}\ \mu\text{m}^{-1}$ and $\alpha = 3$.

Note that the number distribution functions of particles with D $>$ 2 mm can range from 1 to 4 orders of magnitude higher in the initial uniform distribution case compared to the other two cases. At the initial time, the number distribution functions of particles with D $<$ 0.1 mm also span ranges of almost 3 orders of magnitude between the three distributions. This large range of small and large particle concentrations allows this sensitivity test to identify any relationships between concentrations of particles of different sizes with σ.

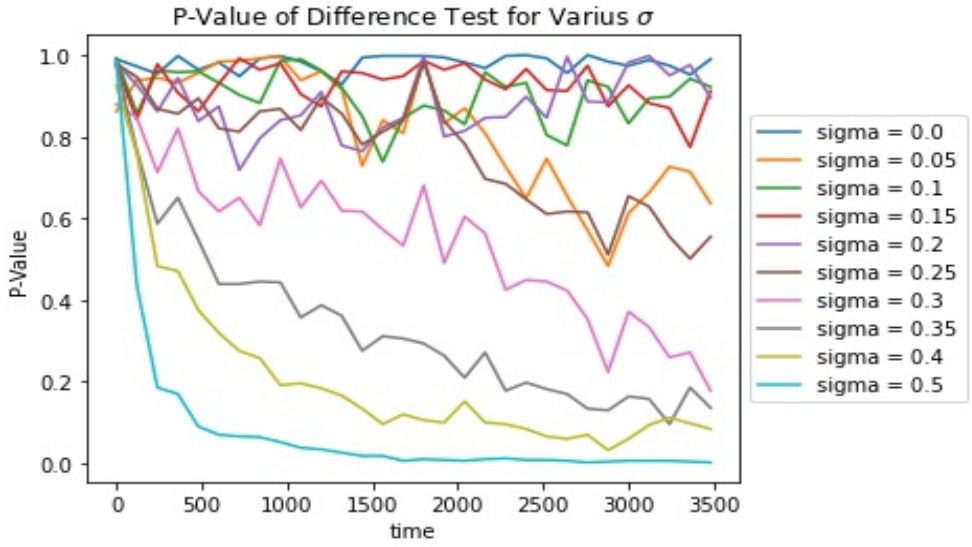

Figure 3.9: P-value generated by the bootstrap statistical analysis comparing each model run to the terminal case (σ = 0 m/s) as a function of time from an initial gamma distribution.

To determine which of the σ values generated equilibrium distributions that were significantly different from the σ = 0.0 m/s, the p-value of the significance test was calculated for the three initial distributions. Unlike the N_t study, the different initial

distributions evolve differently from one another. Comparing how the p-value for each σ runs evolve over time with the initial gamma distribution in Figure 3.9 and with the initial uniform distribution in Figure 3.10. Both of these figures indicate that the models are yet to approach an equilibrium, in the case of the uniform distribution the models are all varying wildly, while the gamma distributions are all very slowly approaching equilibrium. These difference can be understood in terms of the over abundance of particles in specific regions of the DSDs. The uniform distribution has an over abundance of both small particles (D $<$ 0.2 mm) and large particles (D $>$ 3 mm), while the gamma distribution does not have an over abundance of particles in any region of the DSD which results in the slow approach to equilibrium.

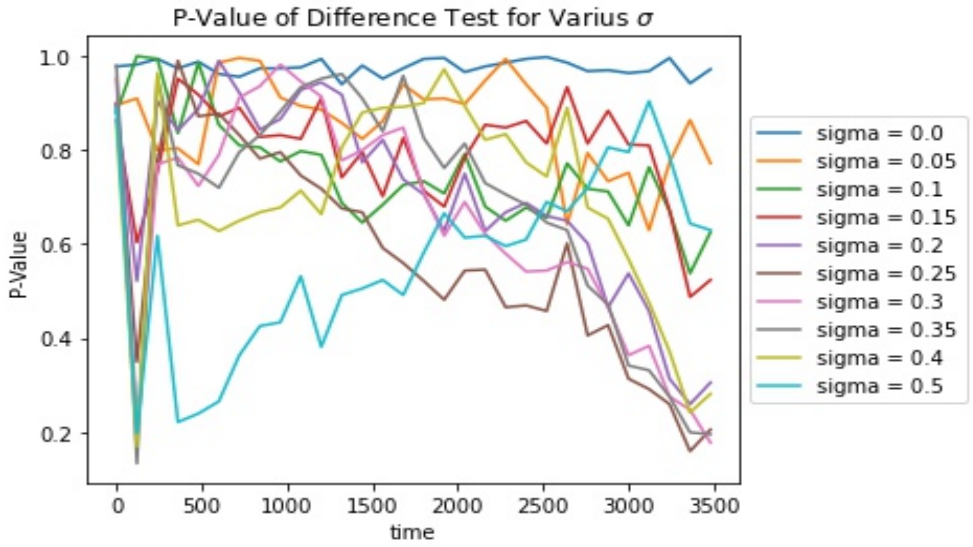

Figure 3.10: P-value generated by the bootstrap statistical analysis comparing each model run to the terminal case (σ = 0 m/s) as a function of time from an initial uniform distribution.

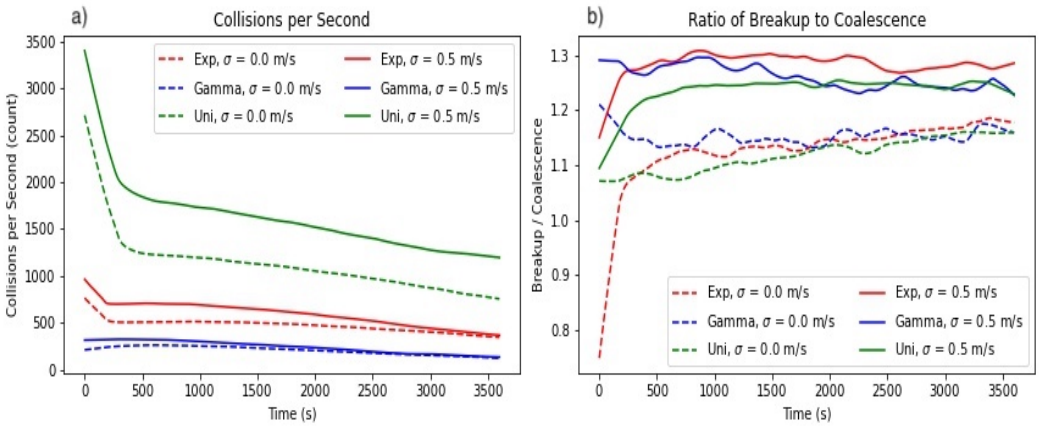

Figure 3.11: a) Number of collisions per second for each of the three initial distributions, with $\sigma = 0.0$ m/s and $\sigma = 0.5$ m/s. b) Ratio of breakup events per second to coalescence events per second for each of the three initial distributions with $\sigma = 0.0$ m/s and $\sigma = 0.5$ m/s

As with the N_t experiment, the relevant collision statistics for the distribution experiment (Figure 3.11) are computed and show that the collisional activity for each simulation varies greatly depending on the initial distribution. In the run initialized with a gamma distribution, the collisional activity within the first 250 seconds is much lower than in the models initialized with uniform or exponential distributions. This relatively low initial collisional activity is due to the gamma distributions lack of particles with D $<$ 0.2 mm. The ratio of breakup to coalescence events in the gamma distribution runs is also more stable over time compared to the other distributions, likely due to the lack of over representation of any size range in the initial distribution. The uniform distribution has a more pronounced initial spike in collisional evolution and over all collisional activity when compared to the exponential distribution. Interestingly, the ratio of breakup to coalescence events in the uniform distribution runs

have different trends depending on the value of σ. For the $\sigma = 0.0$ m/s run, the ratio slowly, roughly linearly increases over the course of the simulation, while the ratio for the $\sigma = 0.5$ m/s run has an initially lower ratio that quickly increases over the first 250 s. This initially lower ratio indicates that for the $\sigma = 0.5$ m/s run there is an increase in the relative importance of coalescence events in the first 250 seconds.

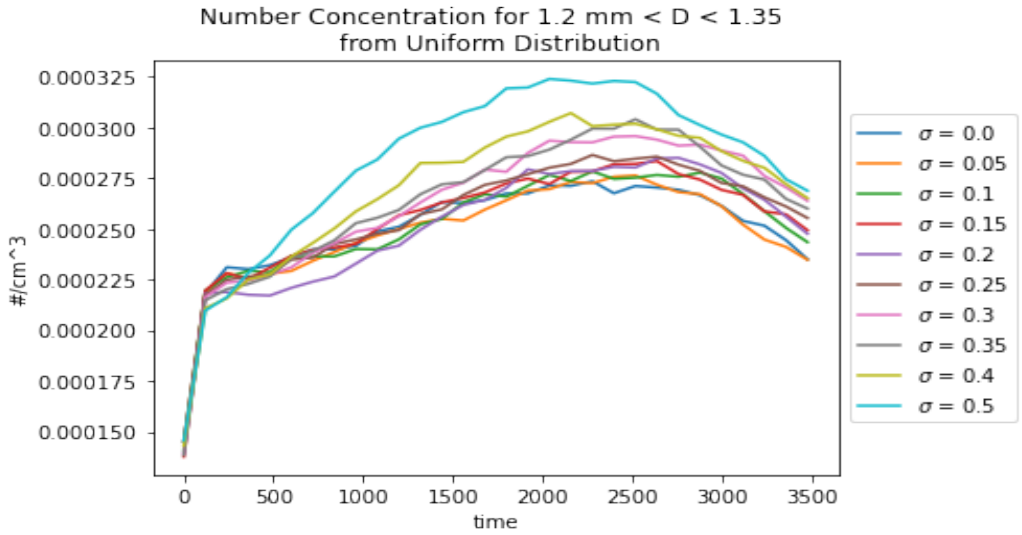

Figure 3.12: Number concentration for all diameters over the course of the evolution of the DSD from an initial uniform distribution.

To better understand the basis of the collision differences, the total number concentrations of the different distributions are shown in Figure 3.12 and Figure 3.13. No critical diameter is found for the gamma distribution since the particles of all sizes follow the same trend. This means that there is no region of the DSD where the various σ runs show a sudden or dramatic deviation in form from one another. The number concentration for the uniform distribution is wildly different due to the over representation of large particles in the initial distribution. The critical diameter D^*

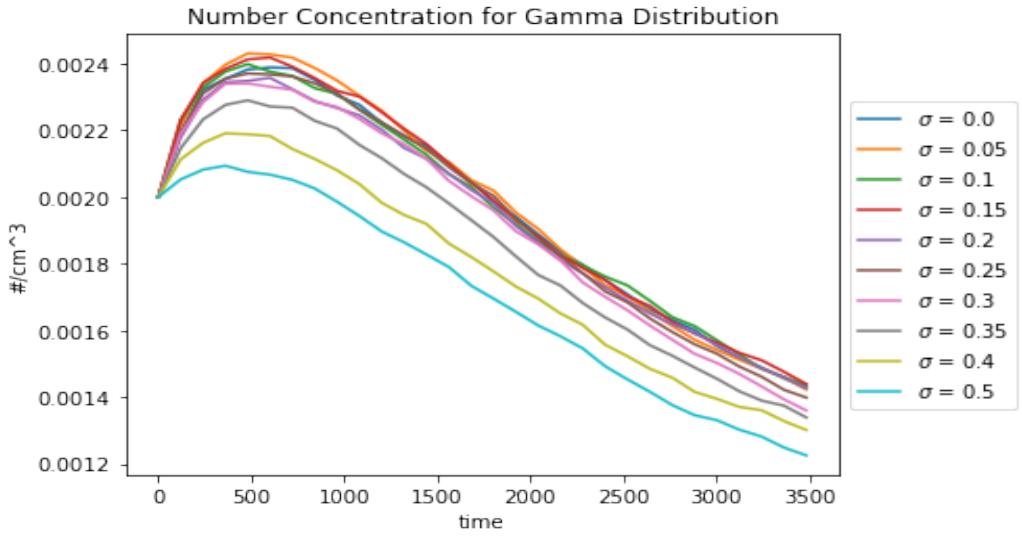

Figure 3.13: Number concentration for all diameters over the course of the evolution of the DSD from an initial gamma distribution.

for the uniform case is 1.3 mm, where models run with lower σ values begin to diverge from models run with higher σ values.

Since D^* for the Uniform case occurs in one of the peaks of the distribution caused by the breakup of large particles, larger values of σ increased the occurrence of breakup events for very large particles with D $>$ 3 mm. This is consistent with the evolution from the initial distribution with an overabundance of large particles towards the equilibrium distribution where those large particles have been broken up through collisions. The deviation between the different σ runs begins after 250 seconds where the ratio of breakup events to coalescence events increases, which further supports the interpretation that the deviation is caused by a higher rate of breakup.

The similarity for all σ values in the model initialized with the gamma distribution indicates that without an over representation of particles in a specific region the

evolution towards the equilibrium distribution occurs smoothly across all regions of the DSD. Unlike in the exponential distribution where there was an overabundance of small particles or the uniform distribution where there was an overabundance of large particles, the gamma distribution did not have any region of the initial DSD with over representation compared to the equilibrium distribution.

3.2 Bias Sensitivity

Figure 3.14 shows the evolution of the DSD for model runs with and without accounting for the functional dependence of μ on D from equation 2.13, the so-called bias term. The equilibrium distribution approached by the unbiased model clearly shows a decrease in number concentration of particles with D $<$ 1.5 mm by 70%, compared to the biased model.

Since the difference between the biased and unbiased fall speed representations is the relative velocity difference between large and small particles, the same approach applied to identify the cause of the differing model behavior under stochastic noise can be applied. This leads to the conclusion that the collision-coalescence-breakup process is responsible for the different model outputs for the biased and unbiased fall speed representations. A comparison of the collision statistics of the two models is shown in figure 3.15. The most obvious difference between the biased and unbiased model results is the decrease in the number of collisions per second in the biased model. For the $\sigma = 0.5$ m/s simulations, the biased model only produced 88% as many collisions over the course of the simulation as the unbiased model. The difference in the number of collisions per second is much less at the end of the simulation where for the lat

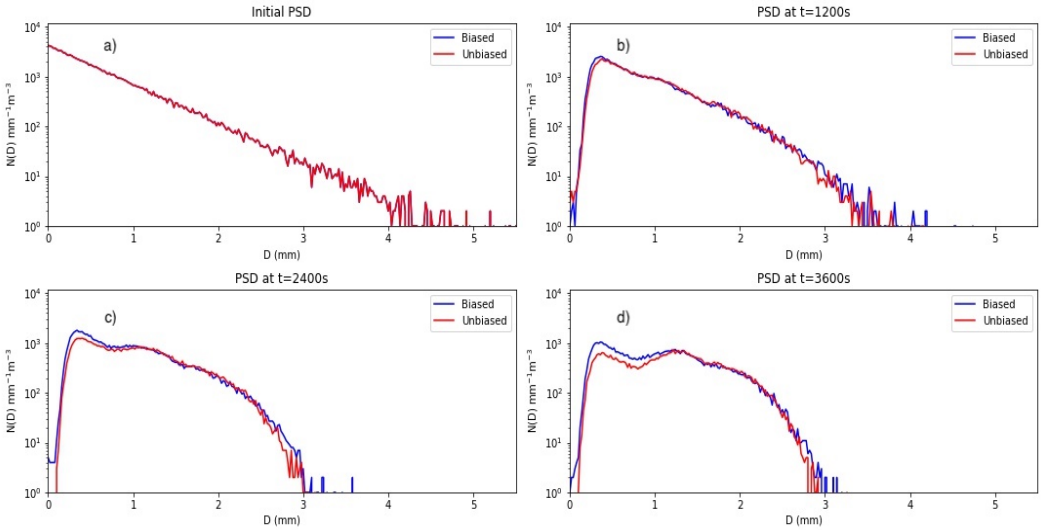

Figure 3.14: Comparison between the biased (blue) and unbiased (red) model drop size distributions. The different models produces significantly different distributions, with the biased model having a notably larger amount of particles of size less than 1.3 mm. The plots show the distributions at different time: a) t = 0 s; b) t = 1200 s; c) 2400 s; d) t = 3600 s

60 seconds all models are within 5.1% of each other. The decrease in the collisional activity of the biased model is caused by the sub-terminal fall speeds of particles with D $>$ 1 mm. Since the large particles fall slower and the small particles fall faster, the number of particles that intersect in each time step is smaller with the bias than without, which reduces the number of collisions per second. The similarity between the biased model with $\sigma = 0.5$ m/s and the unbiased model with $\sigma = 0.3$ m/s is interesting considering the two distributions not only have very similar collisional activity but also very similar distributions, which is not shown. This similarity makes it difficult

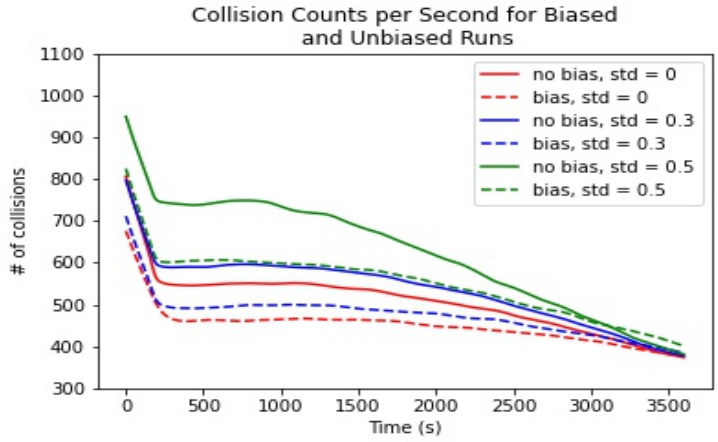

Figure 3.15: Comparison between the biased (dotted lines) and unbiased (solid lines) model collision rates for different σ values. It is clear that for all σ the biased runs have lower collision rates when compared to the unbiased runs.

to differentiate the importance of a specific representation on any observed DSD. This highlights the necessity of high quality fall speed observations to determine the noise and bias to incorporate in the model representation.

Another important difference is the ratio of breakup to coalescence events between the biased and unbiased fall speed representations, which is shown in figure 3.16. The biased model has a lower ratio, meaning that for any given collision event, the probability of coalescence is slightly higher than in the unbiased model. This is most likely a consequence of reducing the number of collisions that particles with D $>$ 1 mm undergo at each time step. The decrease in fall speed for particles with D $>$ 1 mm leads to them interacting with fewer large particles, which are interactions that generally result in breakup. The tendency for larger values of σ to lead to higher ratios of breakup to coalescence events is caused by the increase in interactions of particle with similar sizes

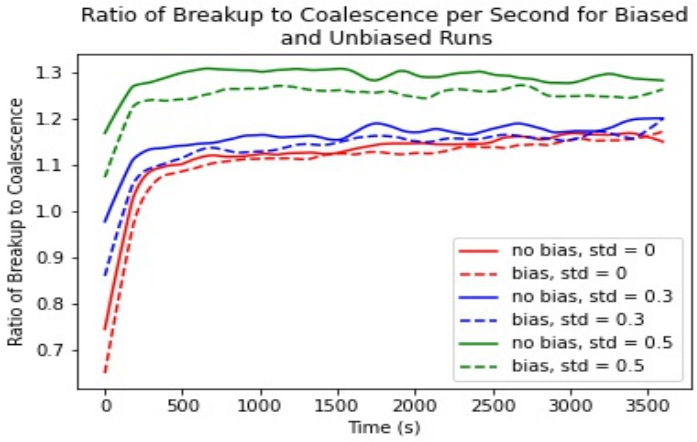

Figure 3.16: Comparison between the biased (dotted lines) and unbiased (solid lines) model ratios of breakup to coalescence events for different σ values. It is clear that for all σ the biased runs have lower ratios when compared to the unbiased runs.

in model runs with high values of σ. These interactions are extremely rare without the inclusion of the noise term and are very likely to result in breakup events.

Comparing the total number concentration N_t and rain rate of the biased and unbiased models in Figure 3.17 shows that the total number concentration is more sensitive to variations in σ than in μ and that the rain rate is more sensitive to variations in μ than in σ. This shows that the bias has a much larger effect on large particles than the standard deviation. Due to the bias' greater effect on larger particles, this representation has the potential to impact bulk properties associated with higher moments such as the rain rate and the radar reflectivity.

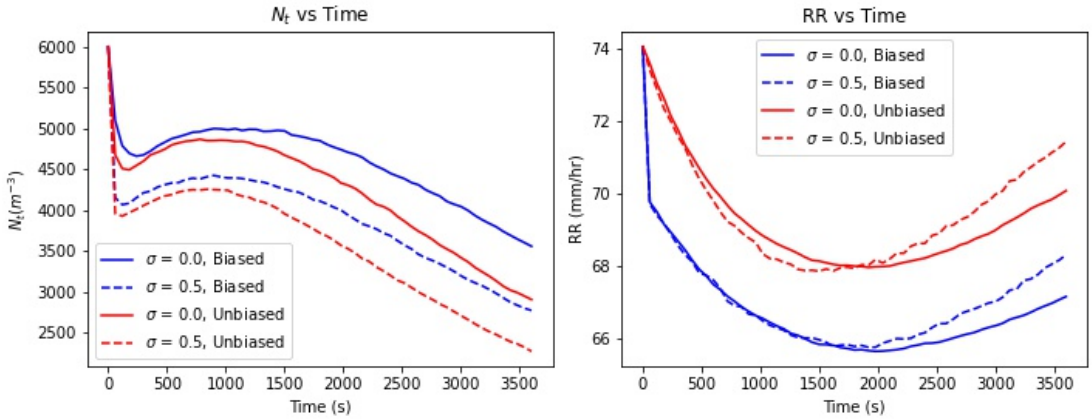

Figure 3.17: a) Comparison between the number concentration of the biased (blue) and unbiased (red) models with different values of σ (dashed: $\sigma = 0.0$ m/s, solid: $\sigma = 0.5$ m/s). b) Same as plot a) but for rain rate instead of number concentration.

3.3 Scaling Sensitivity

The last sensitivity study performed aimed to better understand the impact of particle inertial effects on model behavior. The inertial effects are modeled by a fall speed representation that aims to capture the inertial nature of hydrometeors by scaling the standard deviation of the noise term for particles with diameters greater than some diameter D_s such that particles with D $> D_s$ have smaller standard deviations than those with D $< D_s$. This sensitivity study is motivated by several previous studies that observed a functional dependence of fall speed variance on size (Bringi et al., 2018; Chatterjee et al., 2022; Montero-Martínez and García-García, 2016). This relationship is characterized by a general trend for particles of larger diameters to display a smaller spread in observed fall speeds. Bringi et al. (2018) reported that the standard deviation of 1.3 mm droplets was 1.5 m/s during highly turbulent events, while the standard

deviation of 3 mm droplets during these same events drops to 1 m/s. Montero-Martínez and García-García (2016) reported that the average standard deviation in observed fall speeds tended to decrease with increasing size from 0.4 mm diameter to 2.3 mm diameter droplets for all wind categories they observed (calm, light, and moderate). Data collected by Montero-Martínez and García-García (2016) also indicates that the decrease in average standard deviation of fall speeds is not monotonic with the average standard deviation for droplets larger than 2.3 mm increasing. One important feature of the Montero-Martínez and García-García (2016) and Bringi et al. (2018) data is that the number of droplets of sizes larger than 1.8 mm and 2 mm respectively is very limited, which could result in less reliable standard deviation observations for larger sizes.

Despite these limitations in the observations, it is still important to explore the potential impact of the relationship between fall speed standard deviation and particle size. To represent the observed decrease in standard deviation for larger particles, Equation 2.15 is used. Equation 2.15 uses a scaling factor S that depends on the parameter D_s to control the size at which particles begin to display inertial affects. Equation 2.15 decreases the standard deviation for particles with D $>$ D_s without affecting particles with diameters less than D_s. The model sensitivity to D_s is explored for values of D_s that correspond to particles with diameters around 1.0 mm having significantly less fall speed variance. The values of D_s used are $D_s = 0.25$ mm, which results in halving the fall speed variance for particles with D = 1 mm and $D_s = 0.5$ mm which results in a 70% reduction in fall speed variance for particles with D = 1 mm.

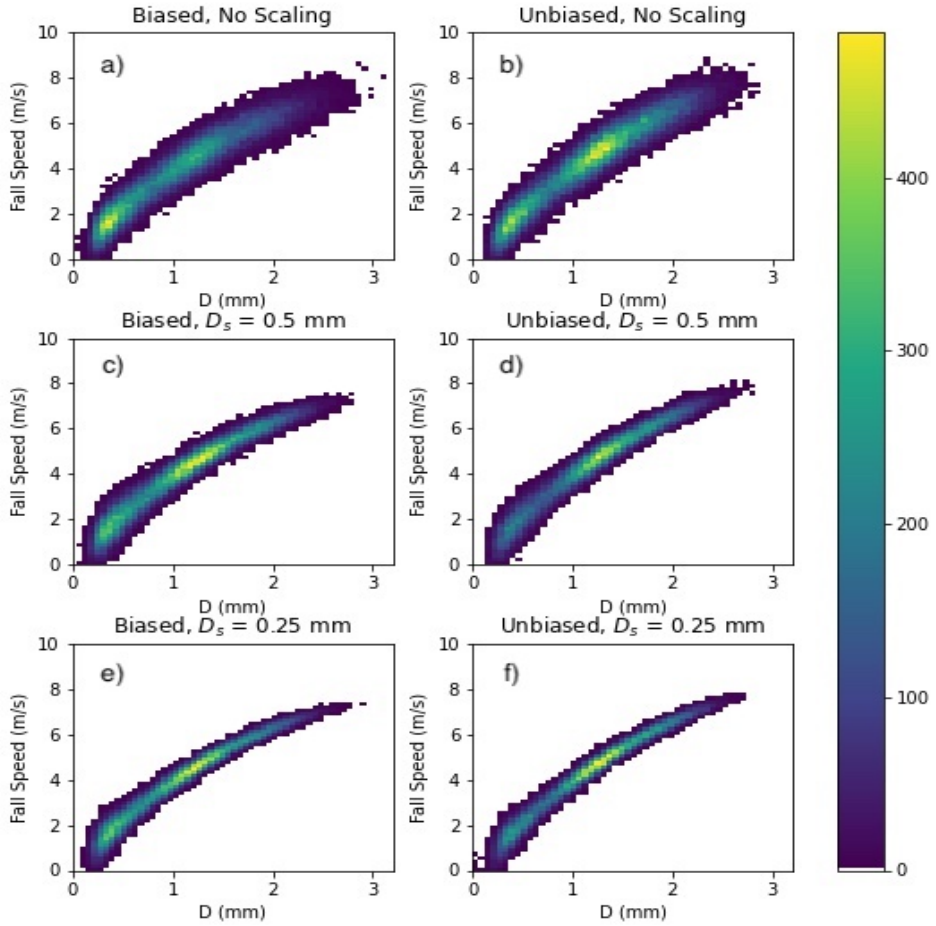

Figure 3.18: Fall speed distributions for the 6 model runs performed in this sensitivity test. The color fill represents the number of particles in each pixel of the diameter vs. fall speed distribution.

The fall speed distributions for the different model runs are shown in figure 3.18. The six model runs used for this sensitivity study include 3 runs with bias and 3 runs

without bias, one run for each with no scaling applied to any particle, one run each with $D_s = 0.5$ mm, and a final set of runs with $D_s = 0.25$ mm. As the scaling parameter D_s increases, the width of the fall speed distributions for large particles drastically decreases as illustrated in the second and third rows of Figure 3.18. From Figure 3.18 the difference between the DSD for the biased and unbiased models is apparent in the regions with the highest density of points in the fall speed distribution. For the biased runs without any scaling applied there are more particles in the smaller peak around 0.4 mm than in the larger peak around 1.3 mm, but the opposite is true for the unbiased, unscaled runs. The scaling runs all increase the relative importance of the large peak compared to the small peak, independent of the bias.

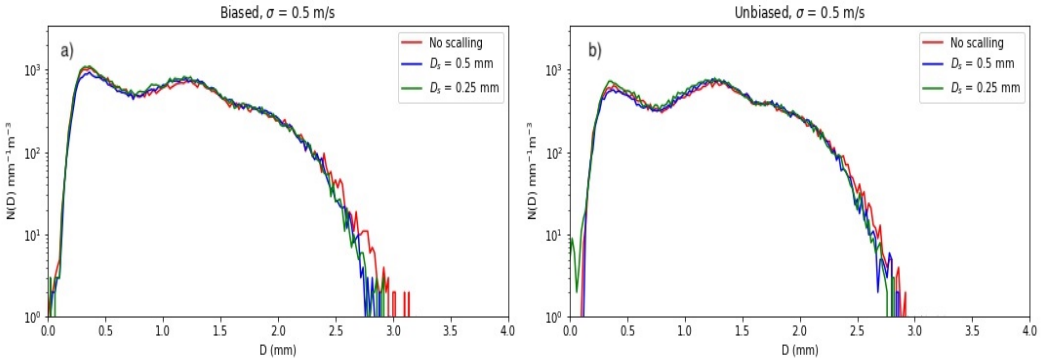

Figure 3.19: a) Equilibrium distribution generated under different values of D_s with bias included and $\sigma = 0.5$ m/s b) Same as left for unbiased model run with $\sigma = 0.5$ m/s.

Figure 3.19 shows the equilibrium distribution approached for model runs with $\sigma = 0.5$ m/s with and without bias. The same trends between the biased and unbiased models persist even with the inclusion of the scaling term. There is a tendency for the

biased models to have fewer large particles than the unbiased models. These differences are less pronounced than the differences between biased and unbiased, or terminal and noise models. The only two minor differences between the DSD generated by the unscaled and scaled models are the increase in the number of particles with diameter around 1.3 mm by 5 % and 4.5 % respectively and a decrease in the number of particles of size greater than 2.4 mm by 5.5 % and 4.1 % respectively. For both the biased and unbiased runs, the scaling term tends to increase the number of particles with diameters around 1 mm and decrease the number of particles with diameters greater than 2.5 mm. The microphysical cause of these two trends is the reduced number of interactions between large particles ($D > 2.5$ mm) and intermediate sized particles (D $\approx$ 1 mm). The number of interactions between large particles and small particles (D < 0.5 mm) is less affected due to the noise of small particles partially offsetting the difference in velocities between large and small particles. With fewer interactions between large and moderate particles there are fewer coalescence events, resulting in more moderate particles and fewer large particles.

Figure 3.20 shows the collision counts for the same model runs shown in figure 3.19. For all values of D_s, the biased model runs have lower collisional activity than the unbiased runs. Within each of these categories, an increase in the D_s parameter results in fewer collisions, meaning that as the number of particles that are scaled increases, the number of collisions occurring per second decreases. This trend is consistent, microphysically speaking, with the results plotted in figure 3.5, where an increase in the standard deviation increases the number of collisions. In figure 3.19 the model runs with the most scaling ($D_s = 0.25$ mm) results in the collisional activity.

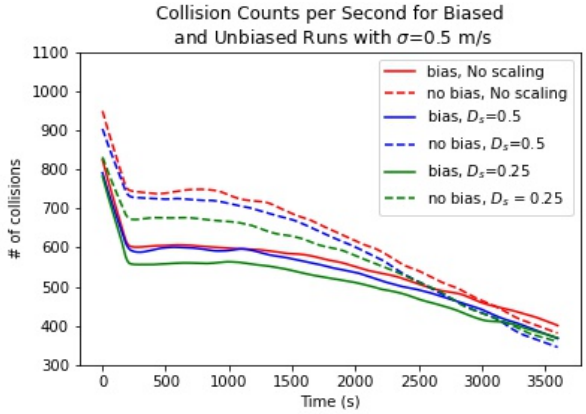

Figure 3.20: Collision counts for the biased (solid lines) and unbiased (dashed lines) model runs with $\sigma = 0.5$ m/s under different values of D_s. For both sets of model runs the $D_s = 0.25$ mm runs have notably lower collision activity compared to the less scaled and unscaled model runs.

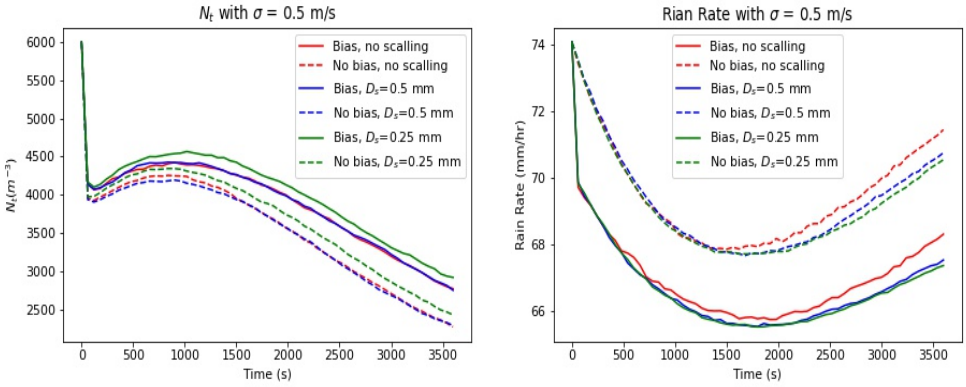

Figure 3.21: a) Number concentration (N_0) as a function of time for each of the 6 simulation runs performed. b) Rain rate as a function of time for each of the 6 model runs performed.

The comparison between the time evolution of number concentration (N_0) and rain rate (RR) for the six model runs is presented in figure 3.21. This comparison summarizes how the fall speed representation affect the bulk cloud moments predicted by the model. The trends present in figure 3.21 are similar to those present in figure 3.17. The inclusion of the scaling term results in greater number concentration while decreasing the rain rate. This is the inverse relationship observed in figure 3.17.

One important caveat to this discussion relates to the physical nature of the scaling term. The term is intended to capture the inertial nature of hydrometeors but the actual acceleration that any given particle experiences in a time step is not directly affected by decreasing the standard deviation of the noise term. To fully represent this physical feature, a more careful treatment of the acceleration during a time step would be required. This crude treatment makes it unsuitable to constrain or estimate the importance of inertia as a physical consideration, but is sufficient to account for the observed decrease in fall speed variance from the available studies.

Chapter 4

Conclusion and Recommended Future Work

For this thesis a novel Lagrangian cloud microphysics model, the Cloud Particle Model (CPM), was used to explore the importance on non-terminal fall speed representations of hydrometeors in warm rain microphysics simulations. The CPM accounted for the most important warm rain microphysical processes including diffusional growth, collision induced coalescence and breakup, and spontaneous breakup. Several different sensitivity studies using non-terminal fall speed representations were performed to better understand how non-terminal fall speeds affect the evolution of drop size distributions (DSDs).

These different fall speed representations were motivated by several observational studies that identified several key features of non-terminal hydrometeor fall speeds. These features include the following; 1) a variance in the fall speed on the order of 0.5 to 1.5 m/s for particles with diameters (D) between 0.4 mm and 3.0 mm which is represented in the CPM by adding a random white noise term to the terminal fall speed; 2) a trend in the variance, such that the variance of larger particles was less than the variance of small particles which is represented in the CPM by scaling the

variance of the noise term for larger particles; and 3) a trend for particles D $>$ 1.3 mm to have sub-terminal fall speeds while particles with D $<$ 0.8 mm tended to have fall speeds that are super-terminal which is represented by adding a functional dependence of the mean of the noise term on the size of particles.

Several sensitivity studies were performed to test the model sensitivity to the different fall speed representations. Firstly the sensitivity of the model to the standard deviation σ of the normal distribution from which the noise term is sampled was tested. From this study the following was revealed:

1. There exists a critical standard deviation, σ^* below which there is no significant difference in the terminal versus non-terminal model output. For the exponential distribution used in this study $\sigma^* = 0.3$ m/s.

2. Higher standard deviation in the noise term resulted in more coalescence events for particles with 0.15 mm $<$ D $<$ 0.4 mm for exponential distributions compared to lower standard deviations.

3. Model runs with different initial distributions demonstrated varying collisional activity due to the difference between those initial distributions and the equilibrium distribution. For example, in initially modeled high collision rate for input exponential distributions were reduced when an equilibrium distribution was approached because the initially high concentration of small drops was reduced.

The model sensitivity to the observed bias was also studied, which showed the following:

1. The inclusion of the bias term results in equilibrium distributions with only 70% as many particles with D $<$ 1.3 mm when compared to equilibrium distributions approached without including the bias.

2. Since the biased model reduced the fall speeds of large particles, they interacted with fewer particles, resulting in a 22 % decrease in the number of collisions per second in the biased model.

3. Higher order moments are more sensitive to variations in the mean of the distribution from which the noise term is drawn μ than in variations in the width of the noise term σ.

The last of the sensitivity studies performed involved experimenting with scaling the width of the distribution from which the noise term in the non-terminal fall speed representations was sampled. The results of this study were as follows:

1. The decrease in the variance in fall speed for large particles results in fewer collision events between particles with large diameters (D $>$ 1.4 mm) and particles with moderate diameters (1.0 mm $< D <$ 1.4 mm)

2. The number of collisions between the large particles and small particles is relatively unaffected due to the small particles higher fall speed variance which somewhat offsets the negative bias of the large particles.

3. The equilibrium distributions that were approached under different scaling conditions were very similar, only varying by only 4 - 5% of each other in total number concentration of particles around the second peak (D $\approx$ 1.3 mm) and 4 - 5 % in total number concentration of particles with D $>$ 2.4 mm.

These sensitivity studies identified specific observational parameters that could be targeted by future observational studies to better constrain the assumptions used in models. It is important to observe the fall speed bias for all particles sizes and especially for large particles, as that would allow field observations of non-terminal fall speeds to be fit to a function. The resulting bias function could then be implemented into the CPM without the inclusion of any noise term. Second, laboratory observations of collision events in a cloud chamber in turbulent environments could complement and explore relationships identified in prior observational and laboratory studies. Such laboratory experiments would allow for the careful study of the causes of non-terminal fall speed variance and allow for greater statistics on the relationship between that variance and particle size, to be established that are difficult to acquire from field observations alone.

Future modeling studies using CPM should focus on understanding how different representations of non-terminal fall speeds directly affect collision, collection, and breakup kernels. This could generate specific corrections to current collision kernels that could be used in broader and more computationally efficient models. Future work with the CPM should also include expanding the model to include mixed phase microphysics, since the fall speed of hydrometeors in mixed and ice phase clouds can have a very different interactions with turbulent environments.

Bibliography

Andrejczuk, M., W. Grabowski, J. Reisner, and A. Gadian, 2010: Cloud-aerosol interactions for boundary layer stratocumulus in the lagrangian cloud model. *Journal of Geophysical Research: Atmospheres*, **115 (D22)**.

Andrejczuk, M., J. Reisner, B. Henson, M. Dubey, and C. Jeffery, 2008: The potential impacts of pollution on a nondrizzling stratus deck: Does aerosol number matter more than type? *Journal of Geophysical Research: Atmospheres*, **113 (D19)**.

Bringi, V., M. Thurai, and D. Baumgardner, 2018: Raindrop fall velocities from an optical array probe and 2-d video disdrometer. *Atmospheric Measurement Techniques*, **11 (3)**, 1377–1384, doi:10.5194/amt-11-1377-2018, URL https://amt.copernicus.org/articles/11/1377/2018/.

Chandrakar, K. K., W. W. Grabowski, H. Morrison, and G. H. Bryan, 2021: Impact of entrainment mixing and turbulent fluctuations on droplet size distributions in a cumulus cloud: An investigation using lagrangian microphysics with a subgrid-scale model. *Journal of the Atmospheric Sciences*, **78 (9)**, 2983 – 3005, doi:https://doi.org/10.1175/JAS-D-20-0281.1, URL https://journals.ametsoc.org/view/journals/atsc/78/9/JAS-D-20-0281.1.xml.

Chatterjee, C., F. Porcù, S. Das, and A. Bracci, 2022: An investigation on super- and sub-terminal drops in two different rain categories and climate regimes. *Remote Sensing*, **14 (11)**, doi:10.3390/rs14112515, URL https://www.mdpi.com/2072-4292/14/11/2515.

Computational and Information Systems Laboratory, 2020: Cheyenne: HPE/SGI ICE XA System (University Community Computing). Boulder, CO: National Center for Atmospheric Research, doi:10.5065/D6RX99HX.

Drake, R., 1972: A general mathematical survey of the coagulation equation. *Topics in current aerosol research (Part 2)*, **3**, 201–376.

Dziekan, P. and H. Pawlowska, 2017: Stochastic coalescence in lagrangian cloud microphysics. *Atmospheric Chemistry and Physics*, **17 (22)**, 13 509–13 520, doi:10.5194/acp-17-13509-2017, URL https://acp.copernicus.org/articles/17/13509/2017/.

Feingold, G. and Z. Levin, 1986: The lognormal fit to raindrop spectra from frontal convective clouds in israel. *J. Climate Appl. Meteor.*, **25 (10)**, 1346–1363.

Foote, G. B. and P. S. D. Toit, 1969: Terminal velocity of raindrops aloft. *Journal of Applied Meteorology and Climatology*, **8 (2)**, 249 – 253, doi:https://doi.org/10.1175/1520-0450(1969)008⟨0249:TVORA⟩2.0.CO;2, URL https://journals.ametsoc.org/view/journals/apme/8/2/1520-0450_1969_008_0249_tvora_2_0_co_2.xml.

Gillespie, D. T., 1972: The stochastic coalescence model for cloud droplet growth. *Journal of the Atmospheric Sciences*, **29 (8)**, 1496–1510.

Gillespie, D. T., 1975: An exact method for numerically simulating the stochastic coalescence process in a cloud. *Journal of the Atmospheric Sciences*, **32 (10)**, 1977–1989.

Grabowski, W. W., H. Morrison, S.-I. Shima, G. C. Abade, P. Dziekan, and H. Pawlowska, 2019: Modeling of cloud microphysics: Can we do better? *Bulletin of the American Meteorological Society*, **100 (4)**, 655–672.

Gunn, R. and G. D. Kinzer, 1949: The terminal velocity of fall for water droplets in stagnant air. *Journal of Atmospheric Sciences*, **6 (4)**, 243 – 248, doi:https://doi.org/10.1175/1520-0469(1949)006⟨0243:TTVOFF⟩2.0.CO;2, URL https://journals.ametsoc.org/view/journals/atsc/6/4/1520-0469_1949_006_0243_ttvoff_2_0_co_2.xml.

Hu, Z. and R. Srivastava, 1995: Evolution of raindrop size distribution by coalescence, breakup, and evaporation: Theory and observations. *Journal of the atmospheric sciences*, **52 (10)**, 1761–1783.

Komabayasi, M., T. Gonda, and K. Isono, 1964: Life time of water drops before breaking and size distribution of fragment droplets. *Journal of the Meteorological Society of Japan. Ser. II*, **42 (5)**, 330–340.

Larsen, M. L., A. B. Kostinski, and A. R. Jameson, 2014: Further evidence for superterminal raindrops. *Geophysical Research Letters*, **41 (19)**, 6914–6918, doi:https://doi.org/10.1002/2014GL061397, URL https://agupubs.onlinelibrary.wiley.com/doi/abs/10.1002/2014GL061397, https://agupubs.onlinelibrary.wiley.com/doi/pdf/10.1002/2014GL061397.

List, R. and G. M. McFarquhar, 1990: The role of breakup and coalescence in the three-peak equilibrium distribution of raindrops. *J. Atmos. Sci.*, **47 (19)**, 2274–2292.

Low, T. B. and R. List, 1982: Collision, coalescence and breakup of raindrops. part i: Experimentally established coalescence efficiencies and fragment size distributions in breakup. *Journal of the Atmospheric Sciences*, **39 (7)**, 1591–1606.

Marshall, J. S. and W. M. K. Palmer, 1948: The distribution of raindrops with size. *J. Meteor.*, **5 (4)**, 165–166.

McFarquhar, G. M., 2004: A new representation of collision-induced breakup of raindrops and its implications for the shapes of raindrop size distributions. *J. Atmos. Sci.*, **61 (7)**, 777–794.

Montero-Martínez, G. and F. García-García, 2016: On the behaviour of raindrop fall speed due to wind. *Quarterly Journal of the Royal Meteorological Society*, **142 (698)**, 2013–2020, doi:https://doi.org/10.1002/qj.2794, URL https://rmets.onlinelibrary.wiley.com/doi/abs/10.1002/qj.2794, https://rmets.onlinelibrary.wiley.com/doi/pdf/10.1002/qj.2794.

Morrison, H., M. Witte, G. H. Bryan, J. Y. Harrington, and Z. J. Lebo, 2018: Broadening of modeled cloud droplet spectra using bin microphysics in an eulerian spatial domain. *Journal of the Atmospheric Sciences*, **75 (11)**, 4005–4030.

Pei, B., F. Y. Testik, and M. Gebremichael, 2014: Impacts of raindrop fall velocity and axis ratio errors on dual-polarization radar rainfall estimation. *Journal of Hydrometeorology*, **15 (5)**, 1849 – 1861, doi:https://doi.org/10.1175/JHM-D-13-0201.1, URL https://journals.ametsoc.org/view/journals/hydr/15/5/jhm-d-13-0201_1.xml.

Ren, W., J. Reutzsch, and B. Weigand, 2020: Direct numerical simulation of water droplets in turbulent flow. *Fluids*, **5 (3)**, doi:10.3390/fluids5030158, URL https://www.mdpi.com/2311-5521/5/3/158.

Rosewell, C. J., 1986: Rainfall kinetic energy in eastern australia. *Journal of Applied Meteorology and Climatology*, **25 (11)**, 1695 – 1701, doi:https://doi.org/10.1175/1520-0450(1986)025⟨1695:RKEIEA⟩2.0.CO;2, URL https://journals.ametsoc.org/view/journals/apme/25/11/1520-0450_1986_025_1695_rkeiea_2_0_co_2.xml.

Rousselet, G. A., C. R. Pernet, and R. R. Wilcox, 2021: The percentile bootstrap: A primer with step-by-step instructions in r. *Advances in Methods*

and Practices in Psychological Science, **4 (1)**, 2515245920911 881, doi:10.1177/2515245920911881, URL https://doi.org/10.1177/2515245920911881, https://doi.org/10.1177/2515245920911881.

Schumann, T., 1940: Theoretical aspects of the size distribution of fog particles. *Quarterly Journal of the Royal Meteorological Society*, **66 (285)**, 195–208.

Scott, W. T., 1968: Analytic studies of cloud droplet coalescence i. *Journal of the atmospheric sciences*, **25 (1)**, 54–65.

Shima, S., K. Kusano, A. Kawano, T. Sugiyama, and S. Kawahara, 2009: The super-droplet method for the numerical simulation of clouds and precipitation: a particle-based and probabilistic microphysics model coupled with a non-hydrostatic model. *Quarterly Journal of the Royal Meteorological Society*, **135 (642)**, 1307–1320, doi:https://doi.org/10.1002/qj.441, URL https://rmets.onlinelibrary.wiley.com/doi/abs/10.1002/qj.441, https://rmets.onlinelibrary.wiley.com/doi/pdf/10.1002/qj.441.

Srivastava, R., 1971: Size distribution of raindrops generated by their breakup and coalescence. *J. Atmos. Sci.*, **28 (3)**, 410–415.

Srivastava, R., 1982: A simple model of particle coalescence and breakup. *J. Atmos. Sci.*, **39 (6)**, 1317–1322.

Testik, F. Y. and A. Bolek, 2023: Wind and turbulence effects on raindrop fall speed. *Journal of the Atmospheric Sciences*, doi:https://doi.org/10.1175/JAS-D-22-0137.1, URL https://journals.ametsoc.org/view/journals/atsc/aop/JAS-D-22-0137.1/JAS-D-22-0137.1.xml.

Thurai, M., M. Schönhuber, G. Lammer, and V. Bringi, 2019: Raindrop shapes and fall velocities in "turbulent times". *Advances in Science and Research*, **16**, 95–101, doi:10.5194/asr-16-95-2019, URL https://asr.copernicus.org/articles/16/95/2019/.

Tzivion, S., G. Feingold, and Z. Levin, 1987: An efficient numerical solution to the stochastic collection equation. *Journal of the atmospheric sciences*, **44 (21)**, 3139–3149.

Ulbrich, C. W., 1983: Natural variations in the analytical form of the raindrop size distribution. *J. Climate and Appl. Meteor.*, **22 (10)**, 1764–1775.

Young, K. C., 1975: The evolution of drop spectra due to condensation, coalescence and breakup. *Journal of the Atmospheric Sciences*, **32 (5)**, 965–973.